



Top-down and facet-selective phase-segregation to construct concave nanocages with strongly coupled hetero-interface for oxygen evolution reaction

Jingchun Wang, Anzhou Yang, Jiatian Li, Keying Su, Yawen Tang, Xiaoyu Qiu ^{*}

Jiangsu Key Laboratory of New Power Batteries, Jiangsu Collaborative Innovation Center of Biomedical Functional Materials, School of Chemistry and Materials Science, Nanjing Normal University, Nanjing 210023, China



ARTICLE INFO

Keywords:

Metal-organic frameworks
Anion etching kinetics
Facet selectivity
Concave heterostructures
Oxygen evolution reaction

ABSTRACT

In this study, a top-down and site-selective anion etching method is devised to stepwisely carve out the NiCo(OH)₂/NiS₂ concave hetero-cages (CHCs) from NiCo Prussian blue analogue (PBA) cube. DFT calculation investigates that the synthetic mechanism is based on anisotropic reactivity of each etchant acted in different facets of NiCo PBA cube and can be generalized to various heterogeneous combinations by tuning their dissolution and reconstitution kinetics (*i.e.* NiCoB/NiS₂, NiCoP/NiS₂). Such strategy without adding extra metal source generates strongly coupled heterointerface with hollow, concave, and ultrathin (~16.2 nm) features, which could harvest abundant active sites, tune the electronic structure, and induce strong lattice strain of Ni. Specifically, the NiCo(OH)₂/NiS₂ CHCs manifest superior activity and stability toward oxygen evolution reaction (OER), with an overpotential of 258.0 mV required for 10.0 mA cm⁻², a Tafel slope of 38.3 mV dec⁻¹, and favorable long-term durability in 1.0 M KOH.

1. Introduction

Oxygen evolution reaction (OER) is one of the pivotal electrocatalytic processes in various electrochemical conversion systems (*i.e.* water splitting units, metal-air batteries), which requires lower activation energy and faster conversion kinetics to achieve maximized power output [1–6]. Developing non-precious-metal-based compounds with controlled architectures and chemical compositions has emerged as a cost-effective way to acquire highly efficient electro-catalysts for OER [7–11]. Metal-organic frameworks (MOFs) have been demonstrated as universal precursors for the fabrication of well-defined OER catalysts owing to their topology-transformable architecture and flexible component adjustability [12–15]. Starting from a MOF, there are two documented strategies to further optimize the conductivity, alter the adsorption behavior, and enhance the intrinsic activity: (i) cation regulation (Co³⁺, Ni²⁺, Mo²⁺), including seed-mediated growth to deposit new metallic compound on a MOF, or cation exchange reaction to carve the skin of a MOF ([M(CN)₆]³⁻, MO₃²⁻) [16–18]. Thereby heterointerfaces could be obtained to invoke synergistic effects of electronic interactions and interface reconstitution [19]. (ii) anion regulation (S²⁻, N³⁻, Se²⁻, OH⁻, etc.), which takes a top-down etching process involves the

breaking of metal/organic linkers and regrowth of covalent bonds to topologically convert MOF into well-structured compound with tailored intrinsic activity [20–23]. Generally, it often leads to highly open structures with enhanced atomic efficiency and shorter diffusion length for charge transport [24,25]. More important, anion etching method no longer introduces any additional metal source, which could fully motivate the utilization of internal metal sites of MOF noumenon, meanwhile accelerate the gas diffusion, electrolyte permeation, and reactants transportation for electro-catalysis [26].

Significant breakthroughs have been achieved on MOF-derived compounds by anion etching, showing specific geometric configurations (*e.g.* nanoframes, nanocages of single or multiple shells, yolk-shell) [27–31]. However, although the structural complexity have been realized, most of them are homogeneous compounds with single-phase composition (hydroxide, sulfide, phosphide, etc.) because the underlying anion etching process is straightforward and exhaustive [32]. Current study on selective anion etching can only leave behind the initial MOF residua as a constituent part of the resultant heterostructures, which is insufficient to act as highly active component for OER [33,34]. Accordingly, it is still difficult to solely using the anion etching for constructing component-heterogeneous MOF derivatives, due to the

* Corresponding author.

E-mail address: 07255@njnu.edu.cn (X. Qiu).

lack of systematic study on the etching rate/position/degree of each anion etchant acted in MOF [35]. Although it has been well recognized that the heterogeneous interface is favorable for OER, which could induce the subtle lattice distortion, modulate the charge separation and migration, and tailor the d-band center of metal sites at the Fermi level [36–38]. Furthermore, since the exquisite superstructures (*i.e.* concave, specific facets) with preferential reactivity are highly desirable for tailoring the intrinsic activity for OER [39,40], on above basis to endow the heterogeneous structure with specific spatial distributions and geometrical architecture is deserved, which could learnt from the success of the precise facets control of noble metal nanocrystals [41].

Herein, we demonstrate a two-step and facet-selective anion etching to construct the NiCo(OH)₂/NiS₂ concave hetero-cages (CHCs) by kinetically controlling the anisotropic reactivity of each etchant acted in fcc-structured NiCo PBA nanocubes. NiCo PBA, a typical MOF, was selected as precursor due to its controllable structure and flexible component adjustability [42,43]. Firstly, an incomplete anion etching by S²⁻ ions is used to preferentially carve the edges and corners of NiCo PBA, forming the NiCo PBA/NiS₂ cross@frame heterocubes. Secondly, the internal PBA cross undergoes second anion etching by OH⁻ to form the ultrathin NiCo(OH)₂/NiS₂ CHCs (forming the NiCoB/NiS₂ CHCs by BO₂⁻ etching and forming the NiCoP/NiS₂ cross@frame heterocubes by PO₄³⁻ etching). Such strategy could avoid the addition of extra metal source, thus endows the products with hollow, concave, and ultrathin (~16.2 nm) features. Meanwhile, EXAFS analysis investigates that the strongly coupled NiCo(OH)₂/NiS₂ heterointerface could increase the lattice disorder, tune the electronic structure, and induce the strong lattice strain of Ni. Inspired by above merits, the NiCo(OH)₂/NiS₂ CHCs manifest superior activity and stability towards OER in alkaline medium.

2. Experimental section

2.1. Chemicals and materials

Nickel(II) nitrate hexahydrate (Ni(NO₃)₂•6H₂O), potassium cobalticyanide(III) (K₃[Co(CN)₆]), sodium citrate trisodium (C₆H₅O₇Na₃), sodium sulfide (Na₂S), sodium hydroxide (NaOH), sodium borohydride (NaBH₄), sodium hydrogen phosphate (NaH₂PO₄), ethanol (C₂H₅OH, 99.7%), and ammonia (NH₃•H₂O, 25%) were purchased from Sigma-Aldrich. Commercial ruthenium dioxide (RuO₂) catalyst was purchased from Johnson Matthey Corporation. All the chemicals mentioned above were of analytical grade and have not been further purified before use.

2.2. Synthesis of 100 nm NiCo PBA nanocube

The NiCo PBA were fabricated on the basis of previous reported work [44] with a slight change. In order to downsize the NiCo PBA under 100 nm region, the reaction temperature was decreased to 0° for slowing down the crystal growth rate. Typically, 87.2 mg of Ni(NO₃)₂ 6H₂O, 132.4 mg of C₆H₅O₇Na₃ and 10 mL of distilled (DI) water were mixed together under ultrasound for 5 min to serve as solution I. Meanwhile, 66 mg of K₃[Co(CN)₆] and 10 mL of DI water were mixed together under ultrasound for 5 min to serve as solution II. Subsequently, solution I and solution II were quickly mixed up and underwent continuous aging for 4 h in the ice-water bath of 0 °C under continuous stirring. Finally, the resultant blue sediments were filtered by centrifugation and washed with ethanol for three times, and dried in an oven at 60 °C.

2.3. Synthesis of NiCo PBA/NiS₂ cross@frame heterocubes

An inexhaustive anion etching by S²⁻ was served to transform NiCo PBA nanocube into NiCo PBA/NiS₂ cross@frame heterocubes according to the following equation:



For a typically synthesis, 20 mg of fresh-made NiCo PBA nanocube and 15 mg of Na₂S were uniformly dispersed in a mixture of 16 mL of DI water and 16 mL of ethanol. After ultrasound for 5 min, the mixture was continuous stirring in a bain-marle at 60 °C. Precisely, the reaction was shut down at 1 h to obtain the NiCo PBA/NiS₂ cross@frame heterocubes. Then the products were collected by centrifugation and washed with DI water and ethanol for three times, and dried in an oven at 60 °C.

2.4. Synthesis of NiCo PBA cross

Typically, 10 mg of the above NiCo PBA/NiS₂ cross@frame heterocubes and 5 mL of NH₃•H₂O were dispersed in 40 mL of DI water. After ultrasound for 5 min, the resultant solution was continuous stirring for 1 h in a bain-marle at 60 °C. Then the products were collected by centrifugation and washed with DI water and ethanol for three times, and dried in an oven at 60 °C.

2.5. Synthesis of NiCo(OH)₂ /NiS₂ concave hetero-cages (CHCs)

An anisotropic anion etching by OH⁻ was served to transform NiCo PBA/NiS₂ cross@frame heterocubes into NiCo(OH)₂/NiS₂ CHCs according to the following equation: Ni₃[Co(CN)₆]₂ + 6OH⁻ → 3Ni(OH)₂ + [Co(CN)₆]³⁻, meanwhile a small amount of dissociative Co³⁺ could couple into the Ni(OH)₂ to form the NiCo(OH)₂. For a typically synthesis, 10 mg of the NiCo PBA/NiS₂ cross@frame heterocubes and 5 mg of NaOH were dispersed in 40 mL of DI water. After ultrasound for 5 min, the resultant solution was continuous stirring for 1 h in a bain-marle at 60 °C. Then the products were collected by centrifugation and washed with DI water and ethanol for three times, and dried in an oven at 60 °C to obtain the NiCo(OH)₂/NiS₂ CHCs.

2.6. Synthesis of NiCoB/NiS₂ CHCs

The protocol was similar to that of the NiCo(OH)₂/NiS₂ CHCs, except that the NaOH was replaced by NaBH₄. Detailedly, 10 mg of the NiCo PBA/NiS₂ cross@frame heterocubes and 5 mg of NaBH₄ were dispersed in 40 mL of DI water. After ultrasound for 5 min, the mixed solution was continuous stirring for 1 h in a bain-marle at 60 °C. Then the products were collected by centrifugation and washed with DI water and ethanol for three times, and dried in an oven at 60 °C.

2.7. Synthesis of NiCoP/NiS cross@frame heterocubes

The protocol was similar to that of the NiCo(OH)₂/NiS₂ CHCs, except that the NaOH was replaced by NaH₂PO₄. Detailedly, 10 mg of the NiCo PBA/NiS₂ cross@frame heterocubes and 5 mg of NaH₂PO₄ were dispersed in 40 mL of DI water. After ultrasound for 5 min, the mixed solution was continuous stirring for 1 h in a bain-marle at 60 °C. Then the products were collected by centrifugation and washed with DI water and ethanol for three times, and dried in an oven at 60 °C.

2.8. Density functional theory (DFT) calculations

We have employed the VASP package [45] to perform all the spin-polarized DFT calculations within the generalized gradient approximation (GGA) using the PBE formulation. We have chosen the projected augmented wave (PAW) potentials [46,47] to describe the ionic cores and take valence electrons into account using a plane wave basis set with a kinetic energy cutoff of 400 eV. Partial occupancies of the Kohn-Sham orbitals were allowed using the Gaussian smearing method and a width of 0.2 eV. A single gamma-point was used for the Brillouin-zone integration. The electronic energy was considered self-consistent when the energy change was smaller than 10⁻⁵ eV. A geometry optimization was considered convergent until the forces on all atoms were smaller than 0.02 eV/Å.

The surface slab modules were build based on the NiCo PBA cell

structure with the lattice constants of $a = b = c = 9.8537 \text{ \AA}$ and $\alpha = \beta = \gamma = 90^\circ$. The number of atomic layers for (111), (110) and (100) surface slabs were 13, 10 and 10, respectively. The size of (111), (110) and (100) surface slabs were $13.9135 \text{ \AA} \times 13.9135 \text{ \AA}$, $9.8383 \text{ \AA} \times 13.9135 \text{ \AA}$ and $9.8383 \text{ \AA} \times 9.8383 \text{ \AA}$, respectively. The slabs were separated by a 15 Å vacuum layer in the z direction between the slab and its periodic images. During structural optimizations of the surface models, the bottom 4 atomic layers were fixed. The adsorption energy (E_{ads}) of an adsorbate A was defined as:

$$E_{\text{ads}} = E_{\text{A/surf}} - E_{\text{surf}} - E_{\text{A}}$$

where $E_{\text{A/surf}}$, E_{surf} and E_{A} refers to the energy of A adsorbed on the surface, the energy of the clean surface, and the energy of A in a $10 \text{ \AA} \times 10 \text{ \AA}$ box, respectively.

2.9. Characterizations

Scanning electron microscopy (SEM) images were performed on Hitachi S4800 at an accelerating voltage of 5 kV. Transmission electron microscopy (TEM) and high-resolution TEM (HRTEM) were acquired on a JEOL JEM-2100F transmission electron microscopy manipulated with an accelerating voltage of 200 kV. High-angle annular dark-field scanning transmission electron microscope (HAADF-STEM) images were acquired on a JEM ARM 200 F microscope operated at 200 kV, which provided a nominal resolution of 0.078 nm. The as-tested nanocrystal dispersions were drop-casted on the thin carbon film and dried under ambient conditions. The X-ray absorption fine structure (XAFS) spectra were measured at the beamline BL14W1 station of the Shanghai Synchrotron Radiation Facility, China. The collected EXAFS data were analyzed using the ATHENA program as implemented in the IFEFFIT software packages according to the standard procedures. The wide-angle X-ray powder diffraction (XRD) patterns were performed on a Model D/MAX-RC X-Ray diffractometer with a Cu K α radiation. X-ray photoelectron spectrometer (XPS) were performed by using a Thermo VG Scientific ESCALAB 250 spectrometer with an Al K α radiator.

2.10. Electrochemical measurements

All the electrochemical measurements were evaluated on a CHI 760E electrochemical analyzer at room temperature. The OER tests were evaluated in 1.0 M KOH electrolyte by employing a three-electrode configuration, including a glassy carbon electrode (GCE, surface area 0.07 cm^2) as the working electrode, a saturated calomel electrode (SCE) as the reference electrode, and a graphite rod as the auxiliary electrode. Potentials in this work were calibrated with respect to reversible hydrogen electrode (RHE) by using the following conversion equation: $E(\text{RHE}) = E(\text{SCE}) + 0.0591 \text{ pH} + 0.242$. The as-tested catalyst ink was prepared by dispersing 2 mg of catalyst in 0.7 mL of DI water and 0.3 mL of ethanol solution. After unremitting ultrasound for 20 min, 10 μL of the suspension was pipetted onto the surface of polished GCE by a micro-pipettor and then dried at 40 °C. Finally, 3 μL of Nafion (5 wt%, Sigma-Aldrich) was dropped on the surface of catalyst-modified GCE and dried again. The linear sweep voltammetry (LSV) were conducted in N_2 -saturated 1.0 M KOH solution at a scan rate of 5 mV s^{-1} without ohmic potential drop (IR) correction. The chronopotentiometry measurement was tested for 12 h at an overpotential of 340 mV.

3. Results and discussion

3.1. Kinetic mechanism for the formation of $\text{NiCo(OH)}_2/\text{NiS}_2$ CHCs

The schematic illustration for the formation of $\text{NiCo(OH)}_2/\text{NiS}_2$ CHCs is elucidated in Fig. 1. The fcc-structured NiCo PBA nanocubes ($\text{Ni}_3[\text{Co}(\text{CN})_6]_2$, a typical MOF) with a side length of 100 nm was served as seed for the two-step anion etching, as the structural features shown in Fig. S1 [48]. Then an incomplete anion etching by S^{2-} ions preferentially took place on the edges and corners to form the NiCo PBA/ NiS_2 cross@frame heterocubes (step i). DFT calculation systematically investigates the adsorption behavior of S^{2-} on (110), (111), and (100) facets of NiCo PBA, respectively. The adsorption strength follows the order of edges > corners > planes (-2.63 eV vs. -1.80 eV vs. -1.43 eV). Accordingly, the etching of S^{2-} preferentially started from the

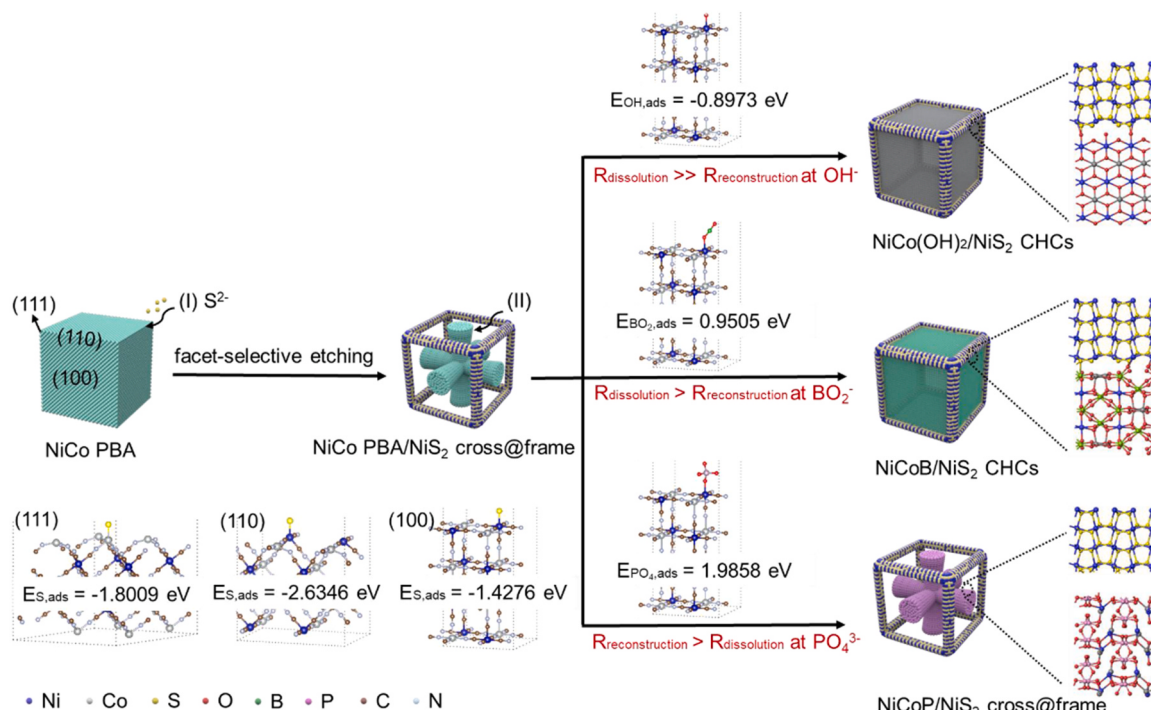


Fig. 1. Schematic illustration showing the formation of $\text{NiCo(OH)}_2/\text{NiS}_2$ CHCs and the proposed etching mechanism from DFT calculations. Step I: facets-selective etching by S^{2-} . Step II: kinetics-controlled etching by OH^- , BO_2^- , PO_4^{3-} , respectively.

edges/corners and the etching rate tended to be faster along the body diagonal direction of the cubes, thus forming an ultrathin NiS₂ frame externally, leaving the internally residual PBA with eight-corners-cut cross-like structure. Following that, the internal PBA cross underwent second anion etching by OH⁻ to form NiCo(OH)₂/NiS₂ CHCs, or form the NiCoB/NiS₂ CHCs by BO₂⁻, and form the NiCoP cross@NiS₂ frame by PO₄³⁻ (step ii). It is worth noting that the theoretical solubility product (K_{sp}) of secondary etching product must be larger than NiS₂ [49]. In this way, the secondary etchant (OH⁻, BO₂⁻, PO₄³⁻) is unable to replace the S²⁻ in the solid phase based on solubility equilibrium, thus avoid the excessive corrosion of as-formed NiS₂ frame. The distinctive shape of final products is attribute to the difference of kinetical dissolution and reconstitution rates induced by OH⁻, BO₂⁻, and PO₄³⁻ on PBA cross, where the adsorption energy follows the order of OH⁻ > BO₂⁻ > PO₄³⁻ (-0.8973 eV vs. 0.9505 eV vs. 1.9858 eV). Obviously, the OH⁻ and BO₂⁻ show stronger adsorption energy relative to PO₄³⁻, which could weaken the relative strength of the interior chemical bonds in PBA cross, thus leading to the decrease of the reaction activation energy of PBA dissolution. In this condition, the metal/organic linkers of NiCo PBA cross were quickly dissolved and then the dissociative Ni, Co, OH⁻ were confined in the NiS₂ frame to take reconstitution, thus forming the NiCo(OH)₂/NiS₂ CHCs ($R_{dissolution} \gg R_{reconstitution}$), or NiCoB/NiS₂ CHCs ($R_{dissolution} > R_{reconstitution}$). In contrast, the week adsorption of PO₄³⁻ on NiCo cross led to a slow kinetic dissolution rate, thus balanced the $R_{dissolution}$ and $R_{reconstitution}$ to gently convert NiCo PBA into NiCoP with cross-like structure remained ($R_{reconstitution} > R_{dissolution}$).

3.2. Characteristics of NiCo(OH)₂/NiS₂ CHCs

The intermediate products induced by S²⁻ etching were collected at different reaction time to show the detailed morphologic evolution (Fig. S2). It displays the etching process started from the edges and corners of NiCo PBA cube, which is basically consistent with the

speculation of DFT calculation. The structural characterization of NiCo PBA/NiS₂ cross@frame heterocubes is investigated by large-scale SEM image (Fig. 2a) and HAADF-STEM image (Fig. 2b). It displays four distinct voids within a square border, indicating the possible formation of cross@frame structure. The wall thickness of external NiS₂ frame was measured to be 16.2 nm (Fig. S3), which is much thinner than most of previously reported frame/cage structures (Table S1). It indicates the ultrathin feature of the NiCo PBA/NiS₂ cross@frame heterocubes derived from the partly etching of PBA cube. The internal cross-like structure is confirmed by etching the external NiS₂ framework. As shown in Fig. S4, the typical concave cross shape could be observed with eight corners cut down. HRTEM images demonstrate obvious light and shade contrast along the center to edge (marked by yellow arrows), further confirming the existence of internal cross structure based on the difference in depth of field (Figs. 2c and S5). By measuring the side length (~90 nm) and diameter of void (~28.5 nm) of NiCo PBA/NiS₂ cross@frame heterocubes, the etching ratio of S²⁻ was determined to be 21.2%. The interplanar spacing was measured to be 0.206 nm at the edges and 0.236 nm at the cross, corresponding to the (110) facets of fcc-NiS₂ and (331) facets of fcc-NiCo PBA, respectively (Fig. S5c). HAADF-STEM image shows the lattice boundary and atomic arrangement along the imageable junction of NiS₂ frame and NiCo PBA cross (Fig. 2d, e). Distinct atom arrangement mode with vacancies/defects could be observed along the boundary, indicative the compositional heterogeneity between the frame and cross. Elemental mapping indicates the outermost distribution of S with a hollow cubic shape, the entire distribution of Ni with a cubic porous shape, and the inner distribution of Co, N and C with a cross shape (Fig. 2f). Such observation points to explicit spatial distribution of inner NiCo PBA cross and epibolic NiS₂ frame, well matching the heterogeneous composition distribution between cross and frame. XRD pattern was performed to investigate the crystal structure of NiCo PBA/NiS₂ cross@frame (Fig. S6). It combines the characteristic peak of both the NiCo PBA (JCPDS no. 89-3738) and

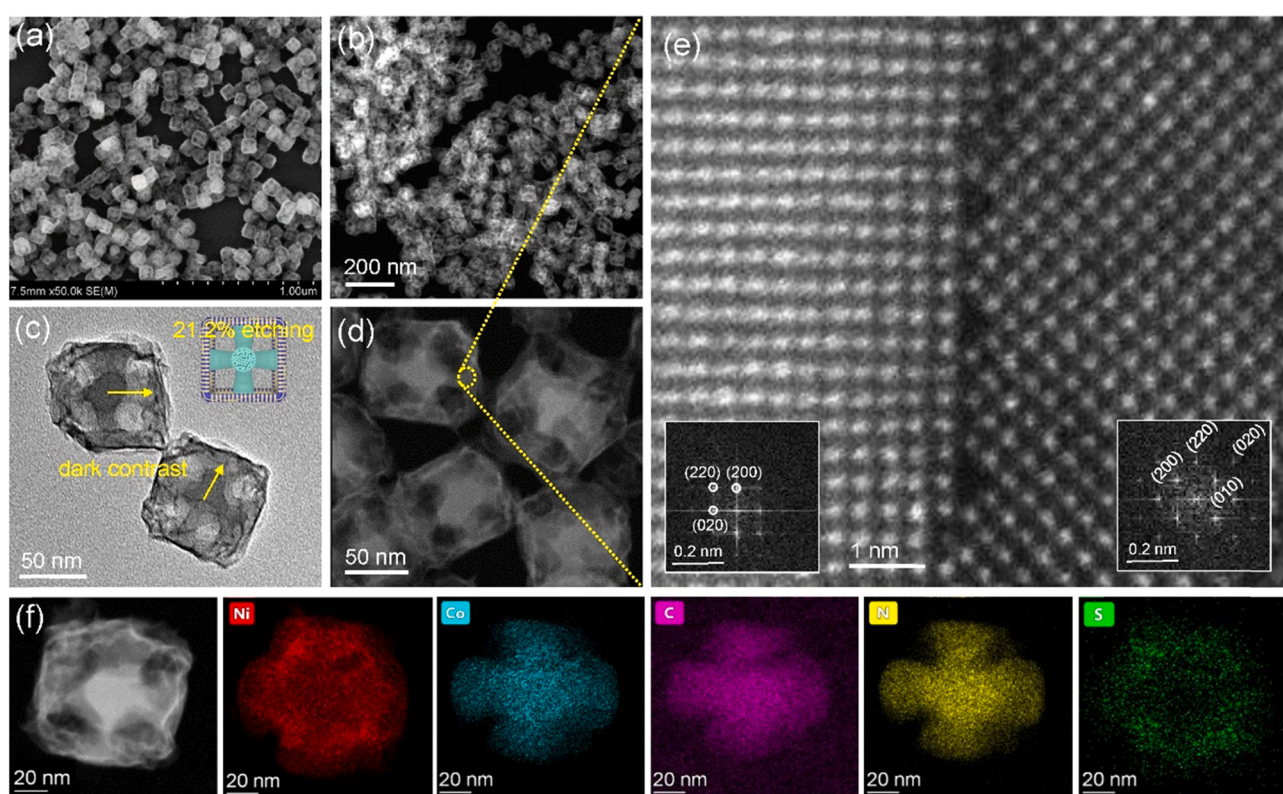


Fig. 2. Characteristics of NiCo PBA/NiS₂ cross@frame heterocubes. (a) SEM image. (b) Large scale HAADF-STEM image. (c) HRTEM image. (d-e) HAADF-STEM image, insert: corresponding FFT patterns. (f) EDS elemental mapping images.

NiS_2 (JCPDS no. 80-0376). XPS demonstrates the existence of Ni, Co, S, C, and N in $\text{NiCo PBA}/\text{NiS}_2$ cross@frame (Fig. S7). Detailedly, the characteristic peak of Ni 2p is located at 855.4 eV ($2p_{3/2}$) and 873.1 eV ($2p_{1/2}$), corresponding to +2 state of Ni in Ni-S and Ni-N. The characteristic peak of Co 2p is located at 781.2 eV ($2p_{3/2}$) and 796.2 eV ($2p_{1/2}$), indicating +3 state in Co-N. The S 2p spectrum reveals two distinct peaks at 161.6 eV ($2p_{3/2}$) and 162.7 eV ($2p_{1/2}$), demonstrating the presence of S^{2-} ions. The main characteristic peak of C 1s and N 1s is located at 284.5 eV and 397.8 eV, respectively, verify the bonding of $\text{C}\equiv\text{N}$. All above results confirm the formation of $\text{NiCo PBA}/\text{NiS}_2$ cross@frame heterocubes, which is originated from selectively and partly carving of NiCo PBA cube.

The secondary anion etching by OH^- is served to convert $\text{NiCo PBA}/\text{NiS}_2$ cross@frame heterocubes into $\text{NiCo(OH)}_2/\text{NiS}_2$ CHCs. As shown in Fig. 3a, SEM image of the products shows a concave structure with cubic configuration. It indicates the disappearance of internal NiCo PBA cross

and the preservation of external NiS_2 frame after OH^- etching. Meanwhile, the wall thickness of outer frameworks was measured to be ca. 16.4 nm, basically consisted with that of the $\text{NiCo PBA}/\text{NiS}_2$ cross@frame heterocubes, indicating the robustness of NiS_2 frame after introducing the OH^- (insert). HRTEM image shown in Fig. 3b displays a cage-like nanostructures consisted of hierarchical flexible nanosheets, which is typical morphology characteristic of the layered hydroxide. HAADF-STEM image is provided to shows the fine structure of $\text{NiCo(OH)}_2/\text{NiS}_2$ CHCs (Fig. 3c). Due to the well-defined dark contrast, where the NiS_2 refers to a bright straight line and the NiCo(OH)_2 refers to dim hierarchical flexible region, the existence of sulfide/hydroxide heterointerface could be confirmed. Fig. 3d clarify the distinctive atomic arrangement in $\text{NiCo(OH)}_2/\text{NiS}_2$ CHCs, that the NiS_2 possesses highly ordered atom arrangement with consistent lattice orientation and well spatial alignment, while the NiCo(OH)_2 part displays highly disordered lattice orientations with anisotropy (Fig. 3e). This result further

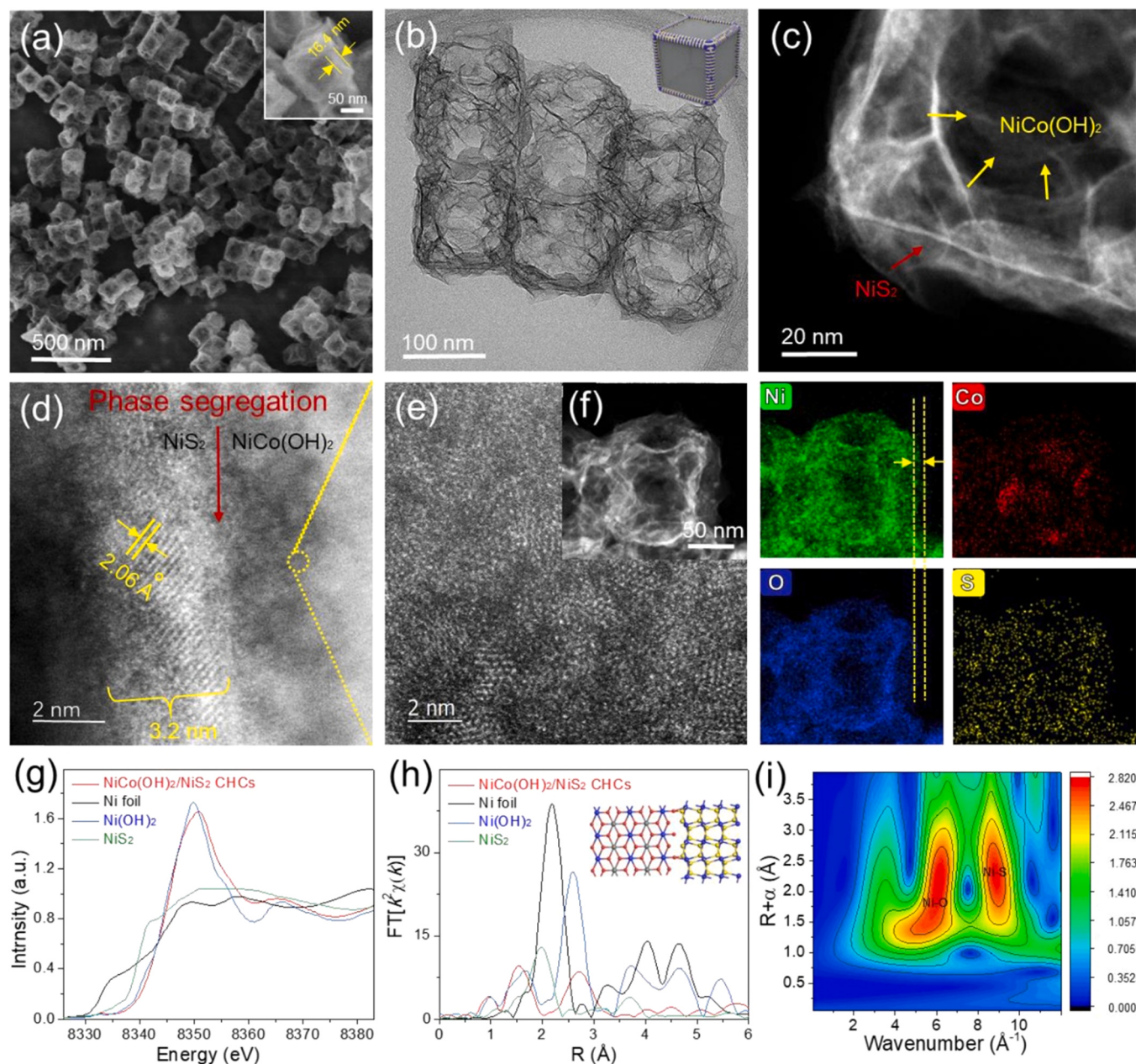


Fig. 3. Characteristics of $\text{NiCo(OH)}_2/\text{NiS}_2$ CHCs. (a) SEM image. (b) HRTEM image. (c-e) HAADF-STEM images. (f) EDS elemental mapping images. (g) Ni K-edge XANES spectra. (h) EXAFS spectra. (i) WT-EXAFS.

confirms the existence of heterointerface consisted of sulfide and hydroxide. Element mapping shows the existence of Ni, O, and S element across the entire concave cages, along with the existence of less Co inside (Fig. 3f). It confirms the successfully hydroxylation to generate the NiCo(OH)₂/NiS₂ CHCs with compositional heterogeneity. XRD pattern of NiCo(OH)₂/NiS₂ CHCs shows newly emerged characteristic peaks at 33.8, 37.7, and 59.9° (refer to (100), (101), (110) facets of hydroxide) and reserved characteristic peaks at 28.2, 39.9, and 59.9° (NiS₂, JCPDS no. 80-0376) compare to those of the NiCo PBA/NiS₂ cross@frame (Fig. S8). It indicates the composition variation after OH⁻ etching. Fig. S9 shows the XPS survey of the NiCo(OH)₂/NiS₂ CHCs, which displays similar electronic structure and valence state at Ni 2p, Co 2p, and S 1s regions compare to those of the NiCo PBA/NiS₂ cross@frame. Nevertheless, the O 1s spectrum is deconvolved into three peaks at 530.4, 531.6, 533.1 eV, corresponding to the lattice oxygen, substituted hydroxyl group, and surface oxygen, respectively, suggesting the formation of hydroxide states.

The Ni K edge XAFS spectroscopy was measured to probe the localized electronic structure and coordination environment in NiCo(OH)₂/

NiS₂ CHCs (Fig. 3g). Obviously, both the pre-edge and K edge position upshift to higher energy values, indicative the reduced electron density around the 3d orbital of Ni sites. It demonstrates the ability of NiCo(OH)₂/NiS₂ CHCs to shuttle the electrons away, thus creating higher-valence-state Ni species. This result also indicates the increased disorder of localized Ni sites compare to bulk NiS₂ and Ni(OH)₂, which could be originated from the chronological interaction of S²⁻ and OH⁻ that induce the rearrangement of electron distribution. The Ni EXAFS demonstrates two prominent peaks at 1.56 Å and 2.70 Å, indicating the variation of coordination environment induced by spectra sulfide and hydroxide (Figs. 3h and S10). Meanwhile, the wavelet transform (WT) contour plot demonstrates maximum intensity at two distinctive areas ($k = 6.0 \text{ \AA}^{-1}$ refers to Ni-O, $k = 8.8 \text{ \AA}^{-1}$ refers to Ni-S), confirming the heterogeneous phase distribution in NiCo(OH)₂/NiS₂ CHCs (Fig. 3i). Table S2 shows the coordination number (CN) of Ni-O (5.9 ± 0.5) and Ni-S (1.4 ± 0.6), which is much lower than bulk Ni(OH)₂ and NiS₂, respectively. It demonstrates a disordered local coordination induced by defects, vacancies from heterointerface [50]. Meanwhile, the average bond length of Ni-O and Ni-S was measured to be 2.03 ± 0.01 and

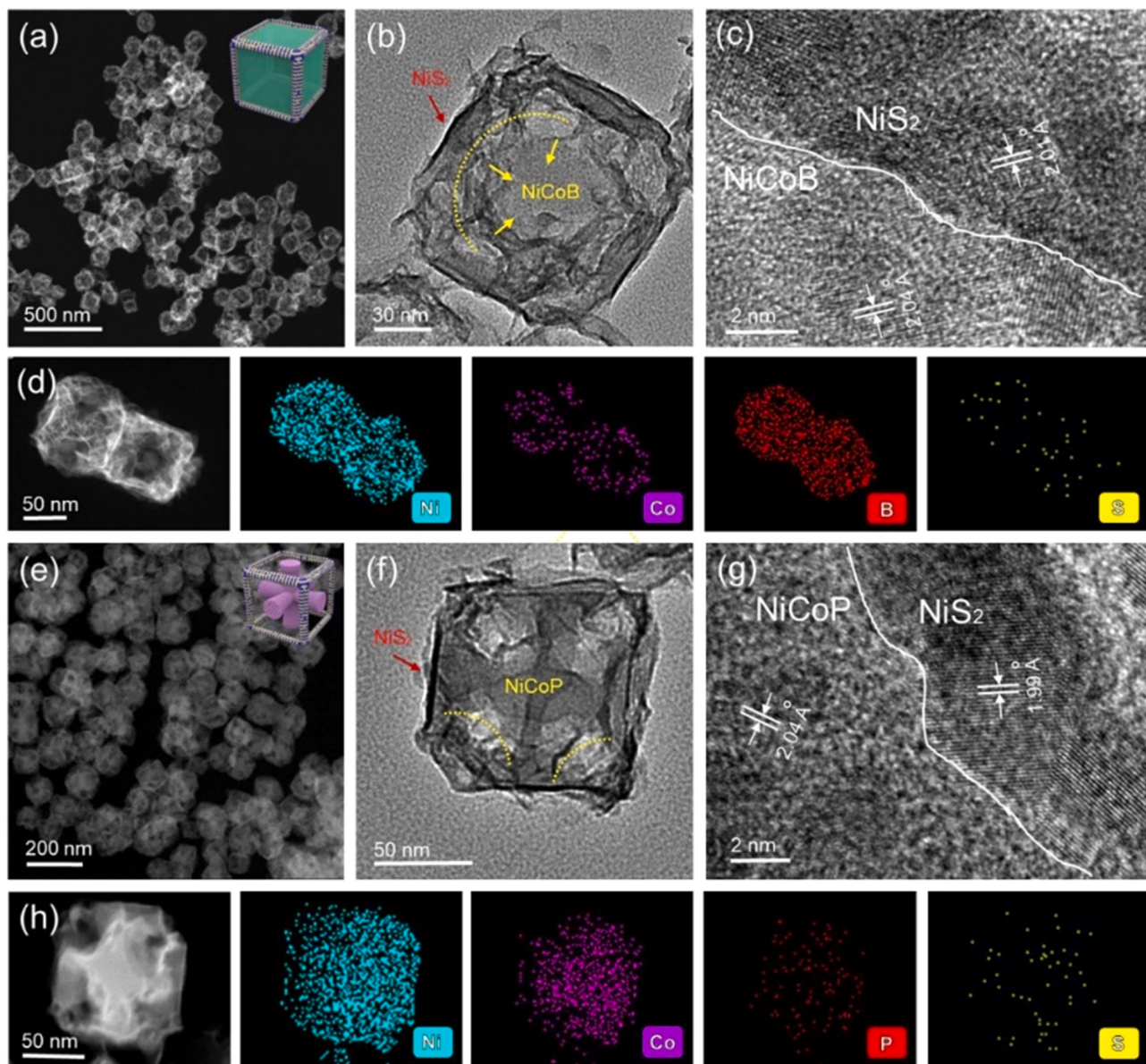


Fig. 4. (a) HAADF-STEM image, (b-c) HRTEM images, (d) EDX element mapping images of NiCoB/NiS₂ CHCs. (e) HAADF-STEM image, (f-g) HRTEM images, (h) EDX element mapping images of NiCoP/NiS₂ cross@frame heterocubes.

2.48 ± 0.01 Å, respectively. Such longer bond distance of Ni-S indicates the existence of lattice strain exerted on crystal lattice of NiS_2 frame, which could be arisen from secondary anion etching of OH^- that causes hybridization and electron transfer into Ni d orbitals [51]. Therefore, above results manifest the successful formation of $\text{NiCo(OH)}_2/\text{NiS}_2$ CHCs and also indicate the establishment of increased lattice chaos, strong lattice strain induced by heterogeneous interface, and the reduced electron density around Ni 3d orbital.

3.3. Universal strategy generalized to the formation of $\text{NiCoB}/\text{NiS}_2$ and $\text{NiCoP}/\text{NiS}_2$

The secondary anion etchant could be generalized to BH_4^- or H_2PO_2^- for constructing sulfide/boride or sulfide/phosphide heterogeneous combinations. Fig. 4a-d demonstrates the structural feature of $\text{NiCoB}/\text{NiS}_2$ CHCs. Both the SEM and HRTEM images display a cage-like structure with the disappearance of internal NiCo PBA cross, which are similar to that of the $\text{NiCo(OH)}_2/\text{NiS}_2$ CHCs. The wall thickness of outer frameworks was measured to be *ca.* 16.5 nm, indicative the ultrathin feature of $\text{NiCoB}/\text{NiS}_2$ CHCs. The interplanar spacing was measured to be 2.01 nm at the frame and 2.04 nm at the cage, corresponding to (110) facets of NiS_2 and (211) facets of NiCoB , respectively. Element mapping verifies the existence of Ni, Co, B, and S element in $\text{NiCoB}/\text{NiS}_2$ CHCs, confirming the formation of NiCoB compound and the well reservation of NiS_2 parts. However, XRD pattern of the $\text{NiCoB}/\text{NiS}_2$ CHCs only displays the characteristic peaks of NiS_2 (JCPDS no. 80-0376), that no obvious characteristic peaks of NiCoB could be observed (Fig. S11). This result could be possibly due to relative low crystallinity degree of NiCoB [52]. XPS survey demonstrates the existence of Ni, Co, B, and S element in $\text{NiCoB}/\text{NiS}_2$ CHCs (Fig. S12). The formation of meta-boron is evidenced by high resolution B 1s spectrum, which displays typical character peak of M-B (187.8 eV), accompanied by B-O peaks (191.7 eV, 192.5 eV). Nevertheless, both the characteristic peak at Ni 2p, Co 2p region negatively shift ~ 0.3 eV as compare to those of NiCo PBA/ NiS_2 cross@frame, indicating that the electronic structure of $\text{NiCoB}/\text{NiS}_2$ CHCs could be tuned by boronizing [53,54].

Fig. 4e-h demonstrates the structural feature of $\text{NiCoP}/\text{NiS}_2$ cross@frame, which was prepared by secondary anion etching of H_2PO_2^- . The products display a typical cross@frame structure with four distinct voids, which are similar to that of the NiCo PBA/ NiS_2 cross@frame. Meanwhile, the wall thickness of external NiS_2 frame was measured to be 16.3 nm, basically constant with that of the NiCo PBA/ NiS_2 cross@frame. The interplanar spacing was measured to be 0.199 nm at the frame and 0.204 nm at the cross, corresponding to the (110) facets of fcc- NiS_2 and (201) facets of fcc- NiP , respectively. Elemental NiCo PBA/ NiS_2 cross@frame mapping images confirm the existence of Ni, Co, P, and S element, confirming the successful phosphating in NiCo PBA/ NiS_2 cross@frame to form the NiCoP compound. Meanwhile, the NiS_2 parts could be partly retained to construct heterointerface with newly-formed NiCoP . The compositional heterogeneity of $\text{NiCoP}/\text{NiS}_2$ cross@frame is confirmed by XRD pattern (Fig. S13). It combines the characteristic peak of both the NiP (JCPDS no. 03-0953, showing a slight shift due to the incorporation of Co) and NiS_2 (JCPDS no. 80-0376). XPS survey demonstrates the co-existence of Ni, Co, P, S element in $\text{NiCoP}/\text{NiS}_2$ cross@frame (Fig. S14). Specifically, the formation of meta-phosphorus is evidenced by the high resolution P 2p spectrum, which displays character peaks at 129.4, 130.5, and 132.7 eV, correspond to the P 2p_{3/2}, P 2p_{1/2}, and P-O species, respectively. Notably, both the characteristic peaks at Ni 2p, Co 2p region show the negatively shift of *ca.* 0.3 eV, which could be derived from the electronic interactions induced by phosphorization. All above results confirm the formation of $\text{NiCoB}/\text{NiS}_2$ CHCs (or $\text{NiCoP}/\text{NiS}_2$ cross@frame) by subsequent B/P etching, which proves the feasibility of stepwise anion etching method for generating well-structured heterogeneous superstructures.

3.4. OER performance of the $\text{NiCo(OH)}_2/\text{NiS}_2$ CHCs

As a proof-of-concept application, the electro-catalytic performance of $\text{NiCo(OH)}_2/\text{NiS}_2$ CHCs was investigated by OER in 1 M KOH electrolyte. As the polarization curves displayed in Fig. 5a, the $\text{NiCo(OH)}_2/\text{NiS}_2$ CHCs exhibit the lowest overpotential of 258 mV to achieve the current density of 10 mA cm^{-2} , while the NiCo PBA/ NiS_2 cross@frame, $\text{NiCoB}/\text{NiS}_2$ CHCs, $\text{NiCoP}/\text{NiS}_2$ cross@frame, and RuO_2 requires larger overpotential of 315 mV, 278 mV, 325 mV, and 347 mV, respectively. Moreover, the $\text{NiCo(OH)}_2/\text{NiS}_2$ CHCs still maintain the superior overpotential at a current density of 20 mA cm^{-2} (Fig. 5b) and afford highest mass activity at an overpotential of 300 mV (Fig. 5c), indicative the maximum catalytic output at minimized overpotentials. The corresponding Tafel plots shown in Fig. 5d implies that $\text{NiCo(OH)}_2/\text{NiS}_2$ CHCs exhibit an ultra-small Tafel slope of 38.3 mV dec^{-1} , which is much lower than that of the NiCo PBA/ NiS_2 cross@frame ($112.4 \text{ mV dec}^{-1}$), $\text{NiCoB}/\text{NiS}_2$ CHCs (38.8 mV dec^{-1}), $\text{NiCoP}/\text{NiS}_2$ cross@frame (42.8 mV dec^{-1}) and RuO_2 ($102.6 \text{ mV dec}^{-1}$), indicating the favorable OER kinetics over the $\text{NiCo(OH)}_2/\text{NiS}_2$ CHCs. Above results reveal that the products after secondary anion etching ($\text{NiCo(OH)}_2/\text{NiS}_2$ CHCs, $\text{NiCoB}/\text{NiS}_2$ CHCs, and $\text{NiCoP}/\text{NiS}_2$ cross@frame) show better OER kinetics than that of the NiCo PBA/ NiS_2 cross@frame. It is because (i) after the secondary etching, the residual PBA cross with low activity was transformed into hydroxide/phosphide/boride component, which hold better intrinsic activity for OER [55,56]; (ii) as investigated by EXAFS, the newly formed sulfide/hydroxides heterointerface could induce the synergistic effects of lattice strain, electronic regulation, and interface engineering. These factors are beneficial for enhancing the catalytic activity [57]. The OER performance of $\text{NiCo(OH)}_2/\text{NiS}_2$ CHCs is also compared with formerly reported noble-metal-free electro-catalysts in alkaline media (Table S3), which exceeds most of them to further confirming its optimal overpotential and Tafel slope. Chronoamperometry measurement was carried out to verify the long-term durability of $\text{NiCo(OH)}_2/\text{NiS}_2$ CHCs. Impressively, the $\text{NiCo(OH)}_2/\text{NiS}_2$ CHCs could maintain the current attenuation continuous operation at 1.57 V for 12 h with 13.8% potential decrease, surpass the other four catalysts (Fig. S15). TEM characterization (Fig. S16) reveals that the concave and hollow structure of the $\text{NiCo(OH)}_2/\text{NiS}_2$ CHCs could be well maintained after chronoamperometry measurement. In addition, TEM images of $\text{NiCoB}/\text{NiS}_2$ CHCs and $\text{NiCoP}/\text{NiS}_2$ cross@frame after chronoamperometry measurement show that the basic structures could be maintained, indicating the well structural robustness of the products after secondary anion etching (Fig. S17). Above results testify the superior OER activity and stability of $\text{NiCo(OH)}_2/\text{NiS}_2$ CHCs, which could be attributed to the following reasons. (i) The NiS_2 presented on frameworks is born with high activity and superior electrical conductivity, meanwhile the NiCo(OH)_2 presented on inner cages endows OER-favored species with straightway conversion efficiency [58]. (ii) The use of NiCo PBA under sub-100 nm, the fractional etching by S^2- (21.2%), and the additive free of metal cation source endows $\text{NiCo(OH)}_2/\text{NiS}_2$ CHCs with ultrathin walls (16.2 nm), which could offer higher surface-area-to-volume ratio and accelerate the gas diffusion, electrolyte transfer, and reactants transportation during OER. (iii) The concave structure not only affords high density of atomic steps/kinks to favor the exposure of active sites, but also maintains structural stability because the internal cage can serve as inner skeleton to support the outer frame [59]. (iv) The strongly coupled sulfide/hydroxides heterointerface could induce the synergistic effects of lattice strain, electronic regulation, and interface engineering [60].

4. Conclusions

In summary, we establish a novel synthetic concept to generate a series of heterostructures (*i.e.* $\text{NiCo(OH)}_2/\text{NiS}_2$, $\text{NiCoB}/\text{NiS}_2$ $\text{NiCoP}/\text{NiS}_2$ with well-defined geometrical configuration (concave, cross@frame)). The kinetical formation mechanism involves: (i) insufficient anion

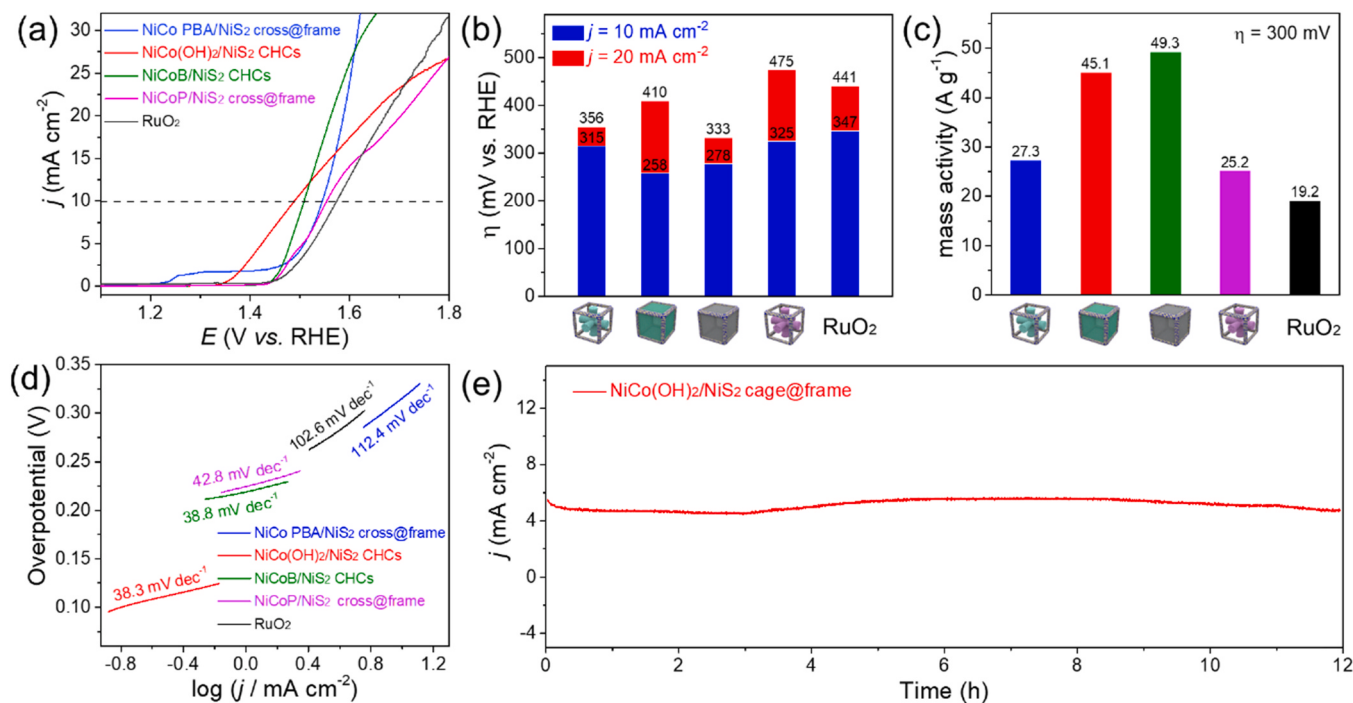


Fig. 5. OER performance of $\text{NiCo(OH)}_2/\text{NiS}_2$ CHCs and controllable samples in 1 M KOH electrolyte with mass loading of 0.27 mg cm^{-2} . (a) LSV polarization curves. (b) Overpotentials at current density of 10 mA cm^{-2} . (c) Mass activity at $\eta = 300 \text{ mV}$. (d) Tafel plots. (e) Chronoamperometric response at an overpotential of 340 mV .

etching by S^{2-} preferentially on edges and corners; (ii) secondary anion etching on internal PBA cross, where the dissolution and reconstitution kinetics are manipulated to determine the final shape. Such design tends to generate strongly coupled heterointerface with hollow, concave, and ultrathin features, which could induce lattice strain, electronic regulation, and interface engineering to boost the OER activity. The two-step and facet-selective anion etching under kinetical control challenges traditional seed-mediated growth to construct well-defined heterogeneous structure, which opens up a new avenue for both fundamental study and realization of various functionalities of non-noble metal nanostructures.

CRediT authorship contribution statement

Jingchun Wang: Methodology, Investigation, Validation, Writing – original draft, Writing – review & editing. **Anzhou Yang:** Formal analysis, Methodology. **Jiatian Li:** Methodology, Investigation, Conceptualization. **Keying Su:** Investigation, Visualization. **Yawen Tang:** Resources, Funding acquisition. **Xiaoyu Qiu:** Supervision, Writing – review & editing, Project administration.

Acknowledgements

X.Q. acknowledge financial support from National Natural Science Foundation of China (21902078), and Natural Science Foundation of Jiangsu Higher Education Institutions of China (19KJB150033). Y.T. acknowledge financial support from National Natural Science Foundation of China (21875112), and Natural Science Foundation of Jiangsu Province (BK20171473). We also thanks to the supports from National and Local Joint Engineering Research Centre of Biomedical Functional Materials and a project sponsored by the Priority Academic Program Development of Jiangsu Higher Education Institutions.

Declaration of competing interest

The authors declare no conflict of interest.

Appendix A. Supporting information

Supplementary data associated with this article can be found in the online version at doi:10.1016/j.apcatb.2021.120727.

References

- [1] S. Zhao, C. Tan, C.-T. He, P. An, F. Xie, S. Jiang, Y. Zhu, K.-H. Wu, B. Zhang, H. Li, J. Zhang, Y. Chen, S. Liu, J. Dong, Z. Tang, Structural transformation of highly active metal-organic framework electrocatalysts during the oxygen evolution reaction, *Nat. Energy* 5 (2020) 881–890.
- [2] C. Liu, J. Qian, Y. Ye, H. Zhou, C.-J. Sun, C. Sheehan, Z. Zhang, G. Wan, Y.-S. Liu, J. Guo, S. Li, H. Shin, S. Hwang, T.B. Gunnoe, W.A. Goddard, S. Zhang, Oxygen evolution reaction over catalytic single-site Co in a well-defined brookite TiO_2 nanorod surface, *Nat. Catal.* 4 (2021) 36–45.
- [3] Z. Liu, G. Wang, X. Zhu, Y. Wang, Y. Zou, S. Zang, S. Wang, Optimal geometrical configuration of cobalt cations in spinel oxides to promote oxygen evolution reaction, *Angew. Chem. Int. Ed.* 59 (2020) 4736–4742.
- [4] C.F. Li, J.W. Zhao, L.J. Xie, J.Q. Wu, Q. Ren, Y. Wang, G.R. Li, Surface-adsorbed carboxylate ligands on layered double hydroxides/metal-organic frameworks promote the electrocatalytic oxygen evolution reaction, *Angew. Chem. Int. Ed.* 60 (2021) 18129–18137.
- [5] J.W. Zhao, C.F. Li, Z.X. Shi, J.L. Guan, G.R. Li, Boosting lattice oxygen oxidation of perovskite to efficiently catalyze oxygen evolution reaction by FeOOH decoration, *Research* 2020 (2020), 6961578.
- [6] H. Xu, Z.X. Shi, Y.X. Tong, G.R. Li, Porous microrod arrays constructed by carbon-confined NiCo@NiCoO_2 core@shell nanoparticles as efficient electrocatalysts for oxygen evolution, *Adv. Mater.* 30 (2018), 1705442.
- [7] H. Jin, H. Zhou, D. He, Z. Wang, Q. Wu, Q. Liang, S. Liu, S. Mu, MOF-derived 3D Fe-N-S co-doped carbon matrix/nanotube nanocomposites with advanced oxygen reduction activity and stability in both acidic and alkaline media, *Appl. Catal. B Environ.* 250 (2019) 143–149.
- [8] J. Chen, Q. Long, K. Xiao, T. Ouyang, N. Li, S. Ye, Z.-Q. Liu, Vertically-interlaced $\text{NiFeP}/\text{MXene}$ electrocatalyst with tunable electronic structure for high-efficiency oxygen evolution reaction, *Sci. Bull.* 66 (2021) 1063–1072.
- [9] X.-P. Li, C. Huang, W.-K. Han, T. Ouyang, Z.-Q. Liu, Transition metal-based electrocatalysts for overall water splitting, *Chin. Chem. Lett.* 32 (2021), <https://doi.org/10.1016/j.ccl.2021.01.047>.
- [10] T. Ouyang, X.T. Wang, X.Q. Mai, A.N. Chen, Z.Y. Tang, Z.Q. Liu, Coupling magnetic single-crystal $\text{Co}_2\text{Mo}_3\text{O}_8$ with ultrathin nitrogen-rich carbon layer for oxygen evolution reaction, *Angew. Chem. Int. Ed.* 59 (2020) 11948–11957.
- [11] W.-K. Han, X.-P. Li, L.-N. Lu, T. Ouyang, K. Xiao, Z.-Q. Liu, Partial S substitution activates NiMoO_4 for efficient and stable electrocatalytic urea oxidation, *Chem. Commun.* 56 (2020) 11038–11041.

- [12] Y. Xiong, Y. Yang, F.J. DiSalvo, H.D. Abruna, Synergistic bimetallic metallic organic framework-derived Pt-Co oxygen reduction electrocatalysts, *ACS Nano* 14 (2020) 13069–13080.
- [13] M. Cai, Y. Li, Q. Liu, Z. Xue, H. Wang, Y. Fan, K. Zhu, Z. Ke, C.Y. Su, G. Li, One-step construction of hydrophobic MOFs@COFs core-shell composites for heterogeneous selective catalysis, *Adv. Sci.* 6 (2019), 1802365.
- [14] S. Lee, S. Oh, M. Oh, Atypical hybrid metal-organic frameworks (MOFs): a combinative process for MOF-on-MOF growth, etching, and structure transformation, *Angew. Chem. Int. Ed.* 59 (2020) 1327–1333.
- [15] T.V.M. Sreekanth, G.R. Dillip, P.C. Nagajyothi, K. Yoo, J. Kim, Integration of Marigold 3D flower-like Ni-MOF self-assembled on MWCNTs via microwave irradiation for high-performance electrocatalytic alcohol oxidation and oxygen evolution reactions, *Appl. Catal. B Environ.* 285 (2021), 119793.
- [16] H. Yang, X. Wang, Secondary-component incorporated hollow MOFs and derivatives for catalytic and energy-related applications, *Adv. Mater.* 31 (2019), 1800743.
- [17] L. Yu, X.Y. Yu, X.W.D. Lou, The design and synthesis of hollow micro-/nanostructures: present and future trends, *Adv. Mater.* 30 (2018), 1800939.
- [18] C. Chen, Y. Tu, Q. Lu, H. Lu, S. Zhang, Y. Zhou, J. Zhang, Z. Liu, Z. Kang, X. Feng, D. Chen, Hierarchical trimetallic Co-Ni-Fe oxides derived from core-shell structured metal-organic frameworks for highly efficient oxygen evolution reaction, *Appl. Catal. B Environ.* 287 (2021), 119953.
- [19] X. Zheng, X. Han, Y. Cao, Y. Zhang, D. Nordlund, J. Wang, S. Chou, H. Liu, L. Li, C. Zhong, Y. Deng, W. Hu, Identifying dense NiSe₂/CoSe₂ heterointerfaces coupled with surface high-valence bimetallic sites for synergistically enhanced oxygen electrocatalysis, *Adv. Mater.* 32 (2020), 2000607.
- [20] X. Li, H. Zhang, P. Wang, J. Hou, J. Lu, C.D. Easton, X. Zhang, M.R. Hill, A. W. Thornton, J.Z. Liu, B.D. Freeman, A.J. Hill, L. Jiang, H. Wang, Fast and selective fluoride ion conduction in sub-1-nanometer metal-organic framework channels, *Nat. Commun.* 10 (2019) 2490.
- [21] Z. Huang, S. Yuan, T. Zhang, B. Cai, B. Xu, X. Lu, L. Fan, F. Dai, D. Sun, Selective selenization of mixed-linker Ni-MOFs: NiSe₂@NC core-shell nano-octahedrons with tunable interfacial electronic structure for hydrogen evolution reaction, *Appl. Catal. B Environ.* 272 (2020), 118976.
- [22] C. Zhu, F. Liu, C. Ling, H. Jiang, H. Wu, A. Li, Growth of graphene-supported hollow cobalt sulfide nanocrystals via MOF-templated ligand exchange as surface-bound radical sinks for highly efficient bisphenol A degradation, *Appl. Catal. B Environ.* 242 (2019) 238–248.
- [23] W.-D. Zhang, H. Yu, T. Li, Q.-T. Hu, Y. Gong, D.-Y. Zhang, Y. Liu, Q.-T. Fu, H.-Y. Zhu, X. Yan, Z.-G. Gu, Hierarchical trimetallic layered double hydroxide nanosheets derived from 2D metal-organic frameworks for enhanced oxygen evolution reaction, *Appl. Catal. B Environ.* 264 (2020), 118532.
- [24] W.-D. Zhang, Q.-T. Hu, L.-L. Wang, J. Gao, H.-Y. Zhu, X. Yan, Z.-G. Gu, In-situ generated Ni-MOF/LDH heterostructures with abundant phase interfaces for enhanced oxygen evolution reaction, *Appl. Catal. B Environ.* 286 (2021), 119906.
- [25] H. Chen, X. Liang, Y. Liu, X. Ai, T. Asefa, X. Zou, Active site engineering in porous electrocatalysts, *Adv. Mater.* 32 (2020), 2002435.
- [26] N. Wang, G. Cheng, L. Guo, B. Tan, S. Jin, Hollow covalent triazine frameworks with variable shell thickness and morphology, *Adv. Funct. Mater.* 29 (2019), 1904781.
- [27] L. Ji, J. Wang, X. Teng, T.J. Meyer, Z. Chen, CoP nanoframes as bifunctional electrocatalysts for efficient overall water splitting, *ACS Catal.* 10 (2019) 412–419.
- [28] P. Wan, H. Xie, N. Zhang, S. Zhu, C. Wang, Z. Yu, W. Chu, L. Song, S. Wei, Stepwise hollow prussian blue nanoframes/carbon nanotubes composite film as ultrahigh rate sodium ion cathode, *Adv. Funct. Mater.* 30 (2020), 2002624.
- [29] M. Wang, Y. Cui, H. Cao, P. Wei, C. Chen, X. Li, J. Xu, G. Sheng, Activating peroxydisulfate with Co₃O₄/NiCo₂O₄ double-shelled nanocages to selectively degrade bisphenol A - a nonradical oxidation process, *Appl. Catal. B Environ.* 282 (2021), 119585.
- [30] X. Mu, H. Yuan, H. Jing, F. Xia, J. Wu, X. Gu, C. Chen, J. Bao, S. Liu, S. Mu, Superior electrochemical water oxidation in vacancy defect-rich 1.5 nm ultrathin trimetal-organic framework nanosheets, *Appl. Catal. B Environ.* 296 (2021), 120095.
- [31] X. Cai, Z. Zeng, Y. Liu, Z. Li, X. Gu, Y. Zhao, L. Mao, J. Zhang, Visible-light-driven water splitting by yolk-shell ZnIn₂S₄-based heterostructure without noble-metal co-catalyst and sacrificial agent, *Appl. Catal. B Environ.* 297 (2021), 120391.
- [32] J. Nai, J. Zhang, X.W.D. Lou, Construction of single-crystalline Prussian blue analog hollow nanostructures with tailororable topologies, *Chem* 4 (2018) 1967–1982.
- [33] L. Sun, Y. Yuan, F. Wang, Y. Zhao, W. Zhan, X. Han, Selective wet-chemical etching to create TiO₂@MOF frame heterostructure for efficient photocatalytic hydrogen evolution, *Nano Energy* 74 (2020), 104909.
- [34] G. Zhang, Y. Li, X. Xiao, Y. Shan, Y. Bai, H.-G. Xue, H. Pang, Z. Tian, Q. Xu, In situ anchoring polymetallic phosphide nanoparticles within porous prussian blue analogue nanocages for boosting oxygen evolution catalysis, *Nano Lett.* 21 (2021) 3016–3025.
- [35] W. Wang, H. Yan, U. Anand, U. Mirsaidov, Visualizing the conversion of metal-organic framework nanoparticles into hollow layered double hydroxide nanocages, *J. Am. Chem. Soc.* 143 (2021), 2002435.
- [36] Y. Wang, S. Chen, J. Zhang, Hierarchical assembly of prussian blue derivatives for superior oxygen evolution reaction, *Adv. Funct. Mater.* 29 (2019), 1904955.
- [37] F. Saleem, Z. Zhang, X. Cui, Y. Gong, B. Chen, Z. Lai, Q. Yun, L. Gu, H. Zhang, Elemental segregation in multimetallic core-shell nanoplates, *J. Am. Chem. Soc.* 141 (2019) 14496–14500.
- [38] Y. He, Y.J. Yoon, Y.W. Harn, G.V. Biesold-McGee, S. Liang, C.H. Lin, V.V. Tsukruk, N. Thadhani, Z. Kang, Z. Lin, Unconventional route to dual-shelled organolead halide perovskite nanocrystals with controlled dimensions, surface chemistry, and stabilities, *Sci. Adv.* 5 (2019) 4424.
- [39] H. Chen, X. Liang, Y. Liu, X. Ai, T. Asefa, X. Zou, Active site engineering in porous electrocatalysts, *Adv. Mater.* 32 (2020), 2002435.
- [40] H. Zhang, M. Jin, Y. Xia, Noble-metal nanocrystals with concave surfaces: synthesis and applications, *Angew. Chem. Int. Ed.* 51 (2012) 7656–7673.
- [41] Z. Li, X. Jiang, X. Wang, J. Hu, Y. Liu, G. Fu, Y. Tang, Concave PtCo nanocrosses for methanol oxidation reaction, *Appl. Catal. B Environ.* 277 (2020), 119135.
- [42] L. Han, X.Y. Yu, X.W. Lou, Formation of Prussian-blue-analog nanocages via a direct etching method and their conversion into Ni-Co-mixed oxide for enhanced oxygen evolution, *Adv. Mater.* 28 (2016) 4601–4605.
- [43] H. Zhang, Q. Jiang, J.H.L. Hadden, F. Xie, D.J. Riley, Pd ion-exchange and ammonia etching of a prussian blue analogue to produce a high-performance water-splitting catalyst, *Adv. Funct. Mater.* 31 (2020), 2008989.
- [44] X.Y. Yu, L. Yu, H.B. Wu, X.W. Lou, Formation of nickel sulfide nanoframes from metal-organic frameworks with enhanced pseudocapacitive and electrocatalytic properties, *Angew. Chem. Int. Ed.* 54 (2015) 5331–5335.
- [45] G. Kresse, J. Furthmüller, Efficient iterative schemes for ab initio total-energy calculations using a plane-wave basis set, *Phys. Rev. B* 54 (1996) 11169–11186.
- [46] G. Kresse, D. Joubert, From ultrasoft pseudopotentials to the projector augmented-wave method, *Phys. Rev. B* 59 (1999) 1758–1775.
- [47] P.E. Blöchl, Projector augmented-wave method, *Phys. Rev. B Condens. Matter* 50 (1994) 17953–17979.
- [48] Q. Shi, C. Zhu, D. Du, Y. Lin, Robust noble metal-based electrocatalysts for oxygen evolution reaction, *Chem. Soc. Rev.* 48 (2019) 3181–3192.
- [49] H.-F. Wang, C. Tang, B. Wang, B.-Q. Li, Q. Zhang, Bifunctional transition metal hydroxysulfides: room-temperature sulfurization and their applications in Zn-air batteries, *Adv. Mater.* 29 (2017), 1702327.
- [50] C. Tsounis, X. Lu, N.M. Bedford, B. Subhash, L. Thomsen, Q. Zhang, Z. Ma, K. K. Ostrikov, A. Bendavid, J.A. Scott, R. Amal, Z. Han, Valence alignment of mixed Ni-Fe hydroxide electrocatalysts through preferential templating on graphene edges for enhanced oxygen evolution, *ACS Nano* 14 (2020) 11327–11340.
- [51] K. Liu, C. Zhang, Y. Sun, G. Zhang, X. Shen, F. Zou, H. Zhang, Z. Wu, E.C. Wegener, C.J. Taubert, J.T. Miller, Z. Peng, Y. Zhu, High-performance transition metal phosphide alloy catalyst for oxygen evolution reaction, *ACS Nano* 12 (2017) 158–167.
- [52] J. Masa, P. Weide, D. Peeters, I. Sinev, W. Xia, Z. Sun, C. Somsen, M. Muhler, W. Schuhmann, Amorphous cobalt Boride (Co₂B) as a highly efficient nonprecious catalyst for electrochemical water splitting: oxygen and hydrogen evolution, *Adv. Energy Mater.* 6 (2016), 1502313.
- [53] Z. Chen, R. Zheng, M. Graś, W. Wei, G. Lota, H. Chen, B.-J. Ni, Tuning electronic property and surface reconstruction of amorphous iron borides via W-P co-doping for highly efficient oxygen evolution, *Appl. Catal. B Environ.* 288 (2021), 120037.
- [54] B. Zhang, F. Yang, X. Liu, N. Wu, S. Che, Y. Li, Phosphorus doped nickel-molybdenum aerogel for efficient overall water splitting, *Appl. Catal. B Environ.* 298 (2021), 120494.
- [55] X. Su, Y. Wang, J. Zhou, S. Gu, J. Li, S. Zhang, Operando spectroscopic identification of active sites in NiFe prussian blue analogues as electrocatalysts: activation of oxygen atoms for oxygen evolution reaction, *J. Am. Chem. Soc.* 140 (2018) 11286–11292.
- [56] P. Zhang, D. Luan, X.W.D. Lou, Fabrication of CdS frame-in-cage particles for efficient photocatalytic hydrogen generation under visible-light irradiation, *Adv. Mater.* 32 (2020), 2004561.
- [57] Q. Ji, Y. Kong, C. Wang, H. Tan, H. Duan, W. Hu, G. Li, Y. Lu, N. Li, Y. Wang, J. Tian, Z. Qi, Z. Sun, F. Hu, W. Yan, Lattice strain induced by linker scission in metal-organic framework nanosheets for oxygen evolution reaction, *ACS Catal.* 10 (2020) 5691–5697.
- [58] D. Chen, C. Chen, Z.M. Baiyee, Z. Shao, F. Ciucci, Nonstoichiometric oxides as low-cost and highly-efficient oxygen reduction/evolution catalysts for low-temperature electrochemical devices, *Chem. Rev.* 115 (2015) 9869–9921.
- [59] D. Liu, Q. Lv, S. Lu, J. Fang, Y. Zhang, X. Wang, Y. Xue, W. Zhu, Z. Zhuang, IrCuNi deeply concave nanocubes as highly active oxygen evolution reaction electrocatalyst in acid electrolyte, *Nano Lett.* 21 (2021) 2809–2816.
- [60] T. Liu, P. Li, N. Yao, G. Cheng, S. Chen, W. Luo, Y. Yin, CoP-doped MOF-based electrocatalyst for pH-universal hydrogen evolution reaction, *Angew. Chem. Int. Ed.* 58 (2019) 4679–4684.